

Structural Characterization of (TBA, H)Ca₂Nb₃O₁₀ Nanosheets Formed by Delamination of a Precursor-Layered Perovskite

F. F. Xu,* Y. Ebina, Y. Bando, and T. Sasaki

National Institute for Materials Science (NIMS), 1-1 Namiki, Tsukuba, Ibaraki 305-0044, Japan

Received: January 31, 2003; In Final Form: June 10, 2003

(TBA, H)Ca₂Nb₃O₁₀ nanosheets have been obtained via delamination of a precursor-layered perovskite KCa₂Nb₃O₁₀. A confined structural characterization was performed using transmission electron microscopy. It has been found that nanosheet fragments with a dimension along the sheet normal consisting of no more than four elementary Ca₂Nb₃O₁₀ slabs usually curve, showing tubular morphology at the periphery. Then cross-sectional view of the nanosheets is possible, which, along with plane-view observations, reveals that most of the present nanosheets are unilamellar with a thickness of only ~ 1.2 nm and high crystallinity is sustained after multiplex synthesis processes including ion exchange, intercalation, and exfoliation. However, chemical analysis indicates partial loss of Ca ions, which appears more severe in “thick” nanosheet aggregates with more than 4-fold stacking. The soft two-dimensional crystallites contain a considerable density of various defects, e.g., vacancies, antiphase domain boundaries, and local structural collapse. Surface structures have been examined by high-resolution electron microscopy, and atomic reconstruction has been observed. Finally, interfacial structures upon restacking of nanosheets are investigated.

Introduction

Recent development of “soft” chemical techniques such as ion exchange, intercalation, and exfoliation^{1–3} has brought about a new class of nanosized material, namely nanosheet either exhibiting unilamellar colloidal nanosheets^{4–9} or curling to form nanoscale tubular “scrolls”.¹⁰ Their high anisotropy in dimensions with a thickness in a nanometer range not only shows an interesting crystallography of two-dimensionality¹¹ but also generates some distinctive physicochemical properties.¹² The nanosheets have usually been obtained by delaminating the precursor-layered materials into their elementary layer units. Hence, titanate and niobate that show lepidocrocite-type and perovskite-type layered structures, respectively, are the two excellent candidates for the synthesis of nanosheet materials having been widely studied.^{1,2,4–8}

Perovskite-type transition-metal oxides exhibit a wide variety of physicochemical properties such as superconductivity,¹³ ferroelectricity,¹⁴ photocatalysis,¹⁵ and magnetoresistance.¹⁶ Thus, their transformation into a two-dimensional nanosheet geometry has attracted progressing attention after the perovskite-type oxides in forms of particles, thin films, and ceramics have been investigated thoroughly. A decade ago, Treacy et al. reported that the layered perovskite HCa₂Nb₃O₁₀ could be prepared to form unilamellar colloidal nanosheets by swelling the interlayer gallery to the point of delamination with a weak, bulky base.⁴ HCa₂Nb₃O₁₀, an ion-exchanged product from KCa₂Nb₃O₁₀, is a weak acid that readily intercalates large organic bases such as tetrabutylammonium hydroxide (TBA⁺OH[−]) in the present study.¹⁷

Thus far, nanosheet materials have been investigated mainly from two points of view. One is the attempt to explore different nanosheet materials from a variety of precursor-layered structures.^{1–10} The other is to understand the state of exfoliated

particles, e.g., the degree of delamination.^{4–7,11,18} However, studies on the structures including crystallinity, microstructures, defects, and surface structures of the exfoliated colloidal sheets are rare.^{4,11,19} This is due to the fact that, in addition to the presence of organic substances absorbed on the nanosheets, the reasons that hinder the electron microscopy study of colloidal nanosheet materials include the difficulty in preparing a cross-section specimen, and consequently it is hard to determine the degree of delamination, i.e., the number of elementary layer units in an individual nanosheet during the plane-view observation. A simulated high-resolution image or plasma-loss region on an electron energy-loss spectrum carries information determined by the specimen thickness. However, the sensitivity of these techniques is not high enough to differentiate a thickness variation in the range of 1.2 nm, the dimension of the Ca₂Nb₃O₁₀ elementary unit along the normal. Treacy et al. have succeeded in determining the extent of exfoliation by examining Rutherford scattered intensities on a high-angle annular dark-field (HAAD) image.⁴ However, the structural details, especially the interfacial and surface structures of an individual perovskite slab or overlapped sheets, could not be obtained by these analytical techniques if only the plane-view observation is employed. In the present transmission electron microscopy (TEM) study of (TBA, H)Ca₂Nb₃O₁₀ nanosheets, it will be seen that nanosheets consisting of no more than four elementary Ca₂Nb₃O₁₀ slabs usually partially curve and show tubular morphology at the periphery. This provides the possibility to observe the cross-sections of nanosheets, which are similar to the TEM characterization of nanotubes. Therefore, simultaneous examination of plane-view and cross-section of an individual nanosheet fragment is possible, and structural information revealed therein is unambiguous and representative of nanosheets with a certain degree of delamination. This paper will report detailed TEM investigations of degree of delamination, crystallinity, microstructure, interface and surface structure, defects, and chemical compositions of the nanosheets with a variety of thickness from

* Corresponding author. E-mail: xu.fangfang@nims.go.jp. Telephone: +81-298-513354 ext. 687. Fax: +81-298-516280.

unilamellar to more than 4-fold stacking. Effects of the present multiplex synthetic routine including ion exchange, intercalation, and exfoliation processes on the final structures of nanosheets will be discussed.

Experimental Section

Materials Preparation. Preparation of the present niobate nanosheets involves delamination of a layered perovskite. Then, a layered perovskite, KCa₂Nb₃O₁₀, was prepared by calcining mixed powders of K₂CO₃, CaCO₃, and Nb₂O₅ (K/Ca/Nb = 1.1:2:3) at 1473 K for 12 h in air. The obtained powder (5 g) was stirred in 200 cm³ of a HNO₃ solution (5 M) for 72 h to replace K⁺ by H₃O⁺. After filtration, the solid was washed with distilled water and then dried in air. The acid-exchanged product was identified to be HCa₂Nb₃O₁₀·1.5H₂O by X-ray powder diffraction method. This HCa₂Nb₃O₁₀·1.5H₂O precursor powder (0.4 g) was dispersed in 100 cm³ of a tetrabutylammonium hydroxide (TBA⁺OH⁻) aqueous solution with a molar ratio of TBAOH/HCa₂Nb₃O₁₀·1.5H₂O = 1:2. The mixture was then shaken vigorously at room temperature for 4 days. A colloidal suspension, i.e., an aggregate of nanosheets of perovskite-type niobate with different thickness, was finally obtained after removing a sediment at the bottom of the flask.

Characterizations. The specimen for TEM examination was prepared by directly dripping droplets of the diluted colloidal suspension onto a carbon-coated Cu microgrid. The microstructural analysis was undertaken on a JEOL3010F field-emission transmission electron microscope (FETEM) operated at 300 kV. A side-entry specimen holder was attached to the microscope with a double-tilting goniometer (±30°). A variety of TEM techniques were used to explicitly examine the microstructure and defect structures of the present nanosheets. They include selected-area electron diffraction (SAD), dark-field (DF) imaging, high-resolution electron microscopy (HREM), and the post-analysis by image simulation. Chemical analysis was performed by X-ray energy dispersive spectroscopy (EDS) on a spectrometer of EX-14S620N, JEOL. Quantification of the EDS spectra was taken using the Cliff–Lorimer ratio technique²⁰ as described by

$$C_A/C_B = k_{AB} \cdot (I_A/I_B) \quad (1)$$

where C_A and C_B denote the weight percents of elements A and B, k_{AB} is the Cliff–Lorimer k factor relating the X-ray intensities I_A for element A and I_B for element B to the chemical concentrations in the irradiated volume. The ratio of the k factor was calculated theoretically for elements Ca, K, and Nb in the present material, giving Ca/K/Nb = 1:1.039:2.789. Image simulation was performed by a software package of MacTempas that uses a multislice method to calculate the electron wave function at the specimen exit surface.²¹ Fourier transformation and image processing of HREM images were done on a DigitalMicrograph (Gatan) platform.²²

Results and Discussion

Since the soft nanosheet material is very sensitive to the electron beam, especially when water and organic molecules are present, the present TEM analysis employed fairly weak illumination which showed flux density no higher than 75 pA/cm². The effects of electron beam illumination and heating on the structures of the present nanosheets have been reported elsewhere.²³ Parts a and b of Figure 1 show the typical morphology and composition of the present perovskite-type niobate nanosheets. The nanosheet fragments show large in-

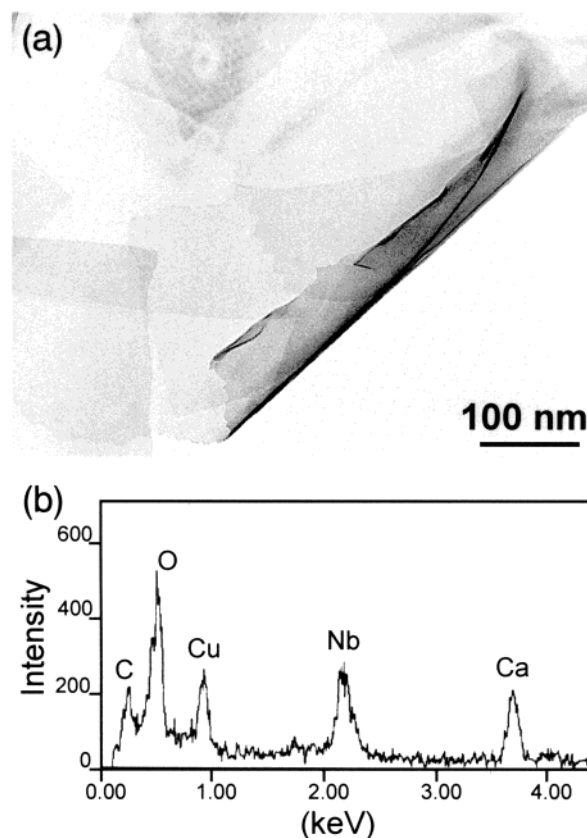


Figure 1. A bright-field TEM micrograph showing the typical morphology of the present perovskite-type niobate nanosheets (a) and a representative EDS spectrum (b).

plane sizes of several micrometers and are usually restacked, a consequence attributed to the TEM specimen preparation from the colloidal suspension. It could be seen that these nanosheets are extremely thin as previewed by their ultralight contrast, which could only be observable via either inserting the smallest objective lens aperture or defocusing a great deal. The exceeding decrease in dimension along the sheet normal leads to striking flexibility for nanosheets. They usually curved or scrolled at the peripheral region, resulting in a tubular morphology where a cross-section of nanosheet is available. Thereafter, the number of elementary layer units along the sheet normal could be easily determined by measuring the cross-section of tubular walls, which is similar to the characterization of nanotubes. Here, we define n as the number of elementary layer units involved in a certain nanosheet fragment.

Unilamellar Nanosheet and Nanosheets with $2 \leq n \leq 4$.

Parts a–d of Figure 2 show the cross-sections of curved nanosheets consisting of one, two, three, and four elementary Ca₂Nb₃O₁₀ layer units, respectively. It should be noted here that the diffraction patterns on the inset of each image were obtained at the inner plane-view region away from the cross-sections. The plane-view diffraction pattern gives explicit structural configurations of parallel-stacked elementary slabs while, in a cross-section view, rotation of elementary slabs about sheet normal upon stacking makes it difficult and usually impossible for each slab to show a certain crystallographic orientation parallel to the electron beam. In Figure 2, the dark dots or fringes refer to the positions of the heavy Nb atoms. The Ca₂Nb₃O₁₀ elementary layer unit contains three NbO₆ octahedral layers along the sheet normal. Thus, every three equidistant dark fringes represent an elementary layer unit. The n value is then obtained simply by counting the number of the triplex fringe.

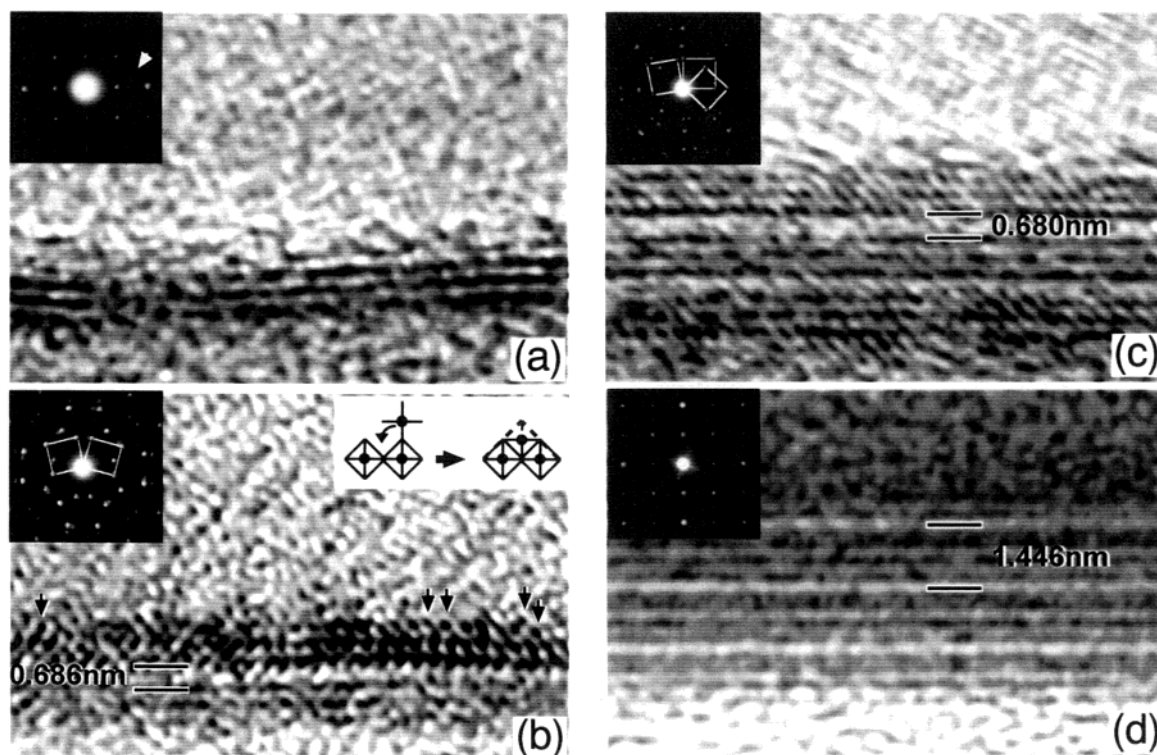


Figure 2. HREM images of cross-sections of (a) unilamellar, (b) duplex, (c) triplex, and (d) quadruplex nanosheets. The attached electron diffraction patterns were obtained from the plane-view region away from the curved periphery for each fragment.

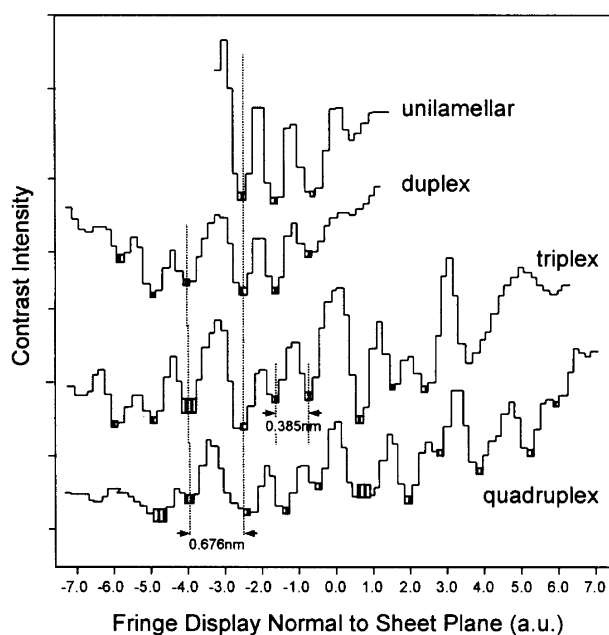


Figure 3. Contrast profiles along the sheet normal for images in Figure 2.

It is revealed in parts b–d of Figure 2 that intervals between the neighboring elementary slabs vary little along the sheet plane within an individual nanosheet or for different nanosheet fragments. From the contrast profiles (Figure 3) along the sheet normal, the distance between the dark fringes from each of the neighboring slabs in the closest vicinity of the interval could be obtained. For the duplex nanosheets, the interval distance varies between 0.680 and 0.698 nm and is peaked at 0.686 nm. The triplex and quadruplex nanosheets exhibit an interval value that is averaged at 0.680 and 0.676 nm, respectively. It is plausible that the intervals reduce with the n value. In any case, the difference is too small to be meaningful.

The interval values for $\text{KCa}_2\text{Nb}_3\text{O}_{10}$,²⁴ $\text{HCa}_2\text{Nb}_3\text{O}_{10}$,¹ and $\text{HCa}_2\text{Nb}_3\text{O}_{10} \cdot 1.5\text{H}_2\text{O}$ ¹ are reported to be 0.701, 0.668, and 0.852 nm, respectively. The EDS analyses, of which an example is shown in Figure 1b that is the EDS spectrum of a triplex nanosheet, did not detect any residual K atoms in the nanosheets with the n value smaller than 5. The K peak otherwise is located in the close vicinity and on the left side of the Ca peak. By noting the atomic ratio $\text{K}/\text{Ca} = 0.5$ in the precursor $\text{KCa}_2\text{Nb}_3\text{O}_{10}$ and the sharp Ca peak in the spectrum, it is apparent that at least the ion-exchange process has gone to completion and the majority of the interlayer potassium ions have been removed. However, since the intervals are only slightly larger than the value of 0.668 nm for $\text{HCa}_2\text{Nb}_3\text{O}_{10}$ and far smaller than 0.852 nm for $\text{HCa}_2\text{Nb}_3\text{O}_{10} \cdot 1.5\text{H}_2\text{O}$, it seems that there is no room for water or TBA molecules to intercalate into the intervals. The plane-view diffraction patterns of the duplex (Figure 2b) and triplex (Figure 2c) nanosheets demonstrate exactly two and three sets of the basic [001] reciprocal lattices, respectively. Therefore, elementary perovskite slabs have been extracted from the previous parallel alignment as in the $\text{HCa}_2\text{Nb}_3\text{O}_{10}$ structure. Two possibilities may give rise to this morphology. One is that the nanosheets were not fully exfoliated even though the rigid interlayer bonding has been broken up. The other possibility involves restacking of unilamellar nanosheet fragments after they were dredged up from the colloidal suspension. Quantitative EDS analyses have revealed an average O/Nb atomic ratio of 6.0 ± 0.8 for unilamellar nanosheets and up to 10.0 ± 1.1 for duplex nanosheets. Moreover, an interesting phenomenon has been observed recently in our in-situ TEM study:²³ the formation of domain boundaries after electron-beam irradiation or heating, which was believed to be the consequence of extraction of interlayer molecules. This phenomenon, together with the ultrahigh O/Nb ratio, may serve as evidence for the actual intercalation of water molecules between the elementary slabs, although the amount of oxygen absorbed on the surfaces on both sides of nanosheet fragments could be different and is

difficult to estimate. The short measured intervals at the cross-section region could possibly be due to the compressive stress upon curving or scrolling, thereby squeezing the interlayer molecules out of the curved region.

Extensive cross-sectional examination indicates that the majority of the present nanosheet fragments are unilamellar although they usually randomly superimpose. Then it is of great interest to know what specific structural and chemical information this thinnest two-dimensional material would give. The sharp round spots in the plane-view electron diffraction pattern (inset in Figure 2a) suggest that a high crystallinity is sustained in the unilamellar nanosheet. At any rate, some weak extra reflections (arrowed) are observable at the $\{1/2, 1/2, 0\}$ positions. The extra reflections at these sites have been proven to arise from the tilting of NbO₆ octahedra around a tetrad along the *c* axis.¹⁹ It is noted that nanosheet aggregates with *n* number larger than 3 (see Figure 2d and ref 19) show prevailing extra spots at either the $\{1/2, 0, 0\}$ or $\{0, 1/2, 0\}$ position, which refers to the tilting of octahedra around the *b* and *a* axes, respectively. Tilting around the *a* and *b* axes takes place as a consequence of movement of interlayer molecules during the exfoliation process. The absence of $\{1/2, 0, 0\}$ and $\{0, 1/2, 0\}$ extra reflections for unilamellar nanosheets suggests the rigid parallel alignment of octahedra along sheet normal is energetically favorable after interlayer interaction disappears. Tilting around the *c* axis leads to reduction in in-plane lattice parameters.¹⁹ The in-plane atomic distances decrease, and the in-plane bonding is strengthened. Such configuration may compensate for the unsaturated bonds due to the lack of nearest-neighbor atoms along *c* direction.

HREM observation (Figure 4a) of unilamellar nanosheets also reveals clear in-plane crystal lattice but with a certain degree of strain. The positions of Nb (dark dots) and Ca (gray dots) atoms are well defined locally on the enlarged image as confirmed by the attached simulated image. However, the image shows contrast characteristic of domains and amorphous regions. The diffractogram (Figure 4b) of the lattice image shows splitting of basic reflections, indicative of the presence of periodic domains. Fourier transformation analysis indicates that these domains are antiphase domains (APBs) with the lattice displacement of *a*/2 or *b*/2. The filtered HREM images, which were inverse-Fourier transformed from different pairs of $\pm\mathbf{g}$ reflections where *g* is (010) for Figure 4c and (100) for Figure 4e, show clearly a lattice shift of half the basic vector between the domains on either side of the boundary. The calculated phase images (Figure 4, d and f) with respect to each of the filtered images further prove the antiphase relation. The weak divergence in the phase contrast among the neighboring antiphase domains results from the strain of the crystal lattice, which alleviates the phase difference. In any case, sharp contrast difference is observable near the antiphase boundaries. Periodic antiphase domains will cause diffraction spots to split.²⁵ The span and the direction of splitting represent the average width of domains and the normal to the domain boundaries, respectively. In Figure 4a, the domains show a square shape consisting of ~ 17 – 20 $\{100\}$ fringes. All the antiphase domains are bounded by (100) and (010) faces. The schematic diagram in Figure 5a illustrates the texture and phase relationship among domains in Figure 4a. The index (0, 0) refers to the original in-plane lattice whereas, for example, (0, 1/2) refers to a *b*/2 lattice shift relative to the (0, 0) domain.

Formation of APB boundaries is believed to occur during the ion-exchange process. This is interpreted via a schematic presentation of ion exchange illustrated in Figure 5b. It should

be noted that the precursor KCa₂Nb₃O₁₀-layered structure involves a *b*/2 lattice displacement between the neighboring elementary perovskite slabs while the ion-exchanged product HCa₂Nb₃O₁₀·1.5H₂O shows rigid parallel packing of slabs without any shift. Thus, ion exchange of K⁺ by H₃O⁺ involves a lattice displacement of half the octahedral tetrad, i.e., *b*/2 of the HCa₂Nb₃O₁₀·1.5H₂O structure. The ion-exchange process sets independently from a variety of sites at the edges of the crystal fragments. Considering two domains on either side of the eventual boundary, as demonstrated on the left part of Figure 5b, we may expect different ion-exchange processes in different domains. In the domain above the eventual APB, the upper elementary slab is supposed to shift to the left by *b*/2 while the second elementary slab remains still. Meanwhile, in the domain below the boundary, the upper layer does not move while the next layer is displaced to the right by *b*/2. When the ion exchange proceeds, the two domains eventually come together and an antiphase domain boundary forms as depicted in Figure 5b.

The presence of an amorphous region in the HREM image implies nonstoichiometric composition for the unilamellar nanosheets. In fact, different chemical compositions other than the nominal Ca₂Nb₃O₁₀ have been observed for different nanosheet aggregates as revealed by quantitative EDS analyses. The Ca/Nb atomic ratio varies from 0.607 to 0.651, with an average value of 0.629 for unilamellar nanosheets. The duplex and triplex nanosheets show a wide range of compositional variation in the range of ~ 0.556 – 0.750 . However, nanosheets with *n* values larger than 3 exclusively show a largely reduced Ca/Nb ratio. For example, the quadruplex nanosheets exhibit a Ca/Nb ratio of 0.464, and nanosheet aggregates with even higher *n* values show an average ratio of 0.420, as will be cited later. This phenomenon seems to be contradictory to the chemical sense and has not been fully understood. In any case, the multiple synthetic processes in the preparation of the present soft ultrathin nanosheets may have been responsible for the compositional nonstoichiometry. The cross-section lattice images in Figure 2 show discontinuity of lattice fringes and blurred contrast, especially in the region near the surfaces and interlayers. Thus, amorphization along with partial loss of species and generation of voids are apparent on the surface and interface regions. Surface reconstruction is observed in some nanosheets. Figure 2b shows displacement of dark dots (Nb atoms) at the surface, as indicated by arrows. As depicted in the schematic drawing attached in Figure 2b, when its nearest in-plane Nb is absent, which can be frequently observed on the surfaces, the Nb atom may “fall” to a position where either an edge-sharing configuration of neighboring octahedra could be employed or the vacant Ca site is occupied so as to compensate for the coordination to the utmost. The structural image shown in the inset of Figure 4a illustrates that some Nb vacancies (marked by circles) occur and some Nb atoms (one of which is marked by an arrow) move to the original Ca sites, as revealed by the contrast variation. Thus, structural damage, especially at the surfaces and interfaces, is generally observed, giving rise to the formation of vacancies and even local structural collapse.

Nanosheets with *n* > 4. With the increase of *n*, the nanosheet aggregates show less flexibility and do not curve at the periphery. This brings difficulty in determining the *n* value. However, these “thick” nanosheet aggregates carry structural information, e.g., defects associated with multiplex synthetic processes. The quantitative EDS analysis reveals high oxygen content and a fairly reduced average Ca/Nb atomic ratio (~ 0.420) compared to the nominal ratio of 0.667. Small amounts

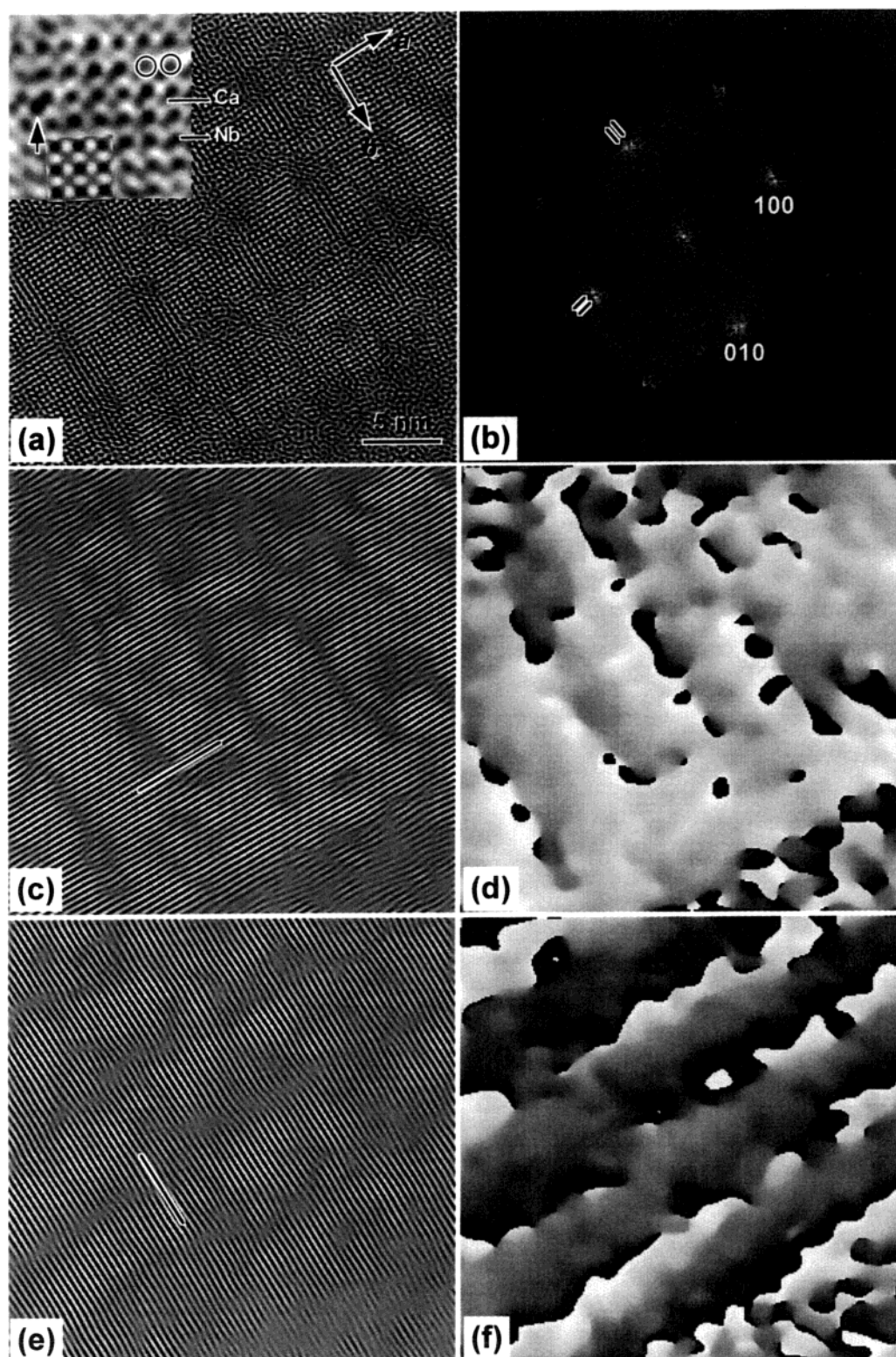


Figure 4. (a) HREM image of a unilamellar nanosheet and (b) its diffractogram showing splitting of reflections, indicative of formation of periodic antiphase domain boundaries. The filtered images by using pairs of (c) $\pm(010)$ and (e) $\pm(100)$ reflections clearly show the lattice shift of half the lattice vector between the neighboring domains. (d) and (f) are the phase images for (c) and (e), respectively, which were calculated using DigitalMicrograph.

of potassium ions from the precursor material have also been detected. Meanwhile, these nanosheet aggregates exhibit high crystallinity and $\text{HCa}_2\text{Nb}_3\text{O}_{10}$ -type crystal structures, as has been revealed by electron diffraction and HREM images.¹⁹ All these results indicate that the nanosheet aggregates have been subject to the ion-exchange process and protonated water molecules have been intercalated. However, the ion-exchange and inter-

calation processes have only been partially fulfilled, leaving a residue of a small amount of potassium ions and making it difficult to be delaminated at the final exfoliation stage.

The common low Ca/Nb atomic ratio, as observed in the present nanosheet material, implies considerable amounts of vacancies at initial Ca sites. A similar phenomenon has been reported for LiNbO_3 bulk perovskite in which heat treatment

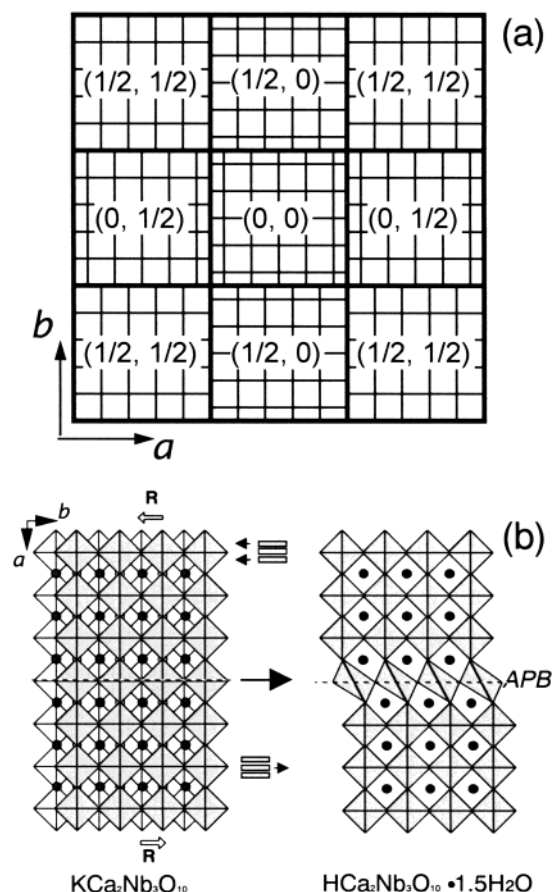


Figure 5. Schematic presentation of (a) the APB texture in Figure 4a and (b) the formation mechanism for APBs, which are believed to be formed in the ion-exchange process.

would partly remove the Li ions out of the material.²⁶ However, this effect is apparently kinetic rather than thermodynamic for the present perovskite nanosheets since no heating has been undertaken during the synthesis and no heating effect is expected in TEM observation when a weak electron beam is employed. Ultrashort distance to the surface in this nanosheet configuration suggests an easier escape of Ca ions once mechanical forces, such as intercalation of interlayer molecules and, more likely, vigorous shaking at the exfoliation process, were employed. Since the HREM images of the present thick nanosheet aggregates show perfect crystal lattices,¹⁹ it seems that only Ca is lost, providing high negative charge to the nanosheets. This phenomenon indicates weak bonding of interstitial Ca atoms to the NbO₆ octahedra. As has been revealed above, delaminated nanosheets ($n \leq 4$) show less deviation from nominal composition than the nanosheet aggregates. Thus, the delaminated nanosheets could have been obtained from fully TBA-intercalated layered material, which suffered little from the vigorous mechanical shaking and were easily exfoliated. However, poorly intercalated nanosheet aggregates have been subject to severe mechanical impact before they could be delaminated. Considerable damage occurs, resulting in extraction of Ca ions.

Dark-field imaging of the nanosheet aggregates reveals considerable density of APBs (Figure 6) that have been believed to be formed during the ion-exchange process. It can be seen that the antiphase boundaries always extend in $\langle 010 \rangle$ or $\langle 100 \rangle$ direction rather than randomly. This configuration may indicate a low-energy boundary of $\{100\}$ APBs and/or a kinetically favored proceeding direction of ion exchange along the a and b axes. Extensive plane-view TEM examination has not

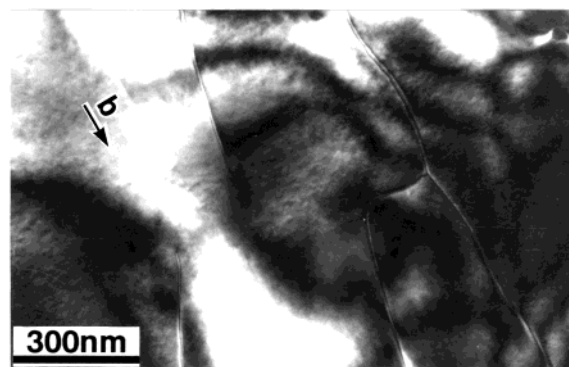


Figure 6. DF image of APBs in a "thick" nanosheet aggregate, which was imaged by a $\langle 020 \rangle$ reflection vector that is parallel to the arrow on the figure.

discovered dislocation lines in the present nanosheet material. However, this does not exclude the possible presence of dislocation cores with Burger's vector lying on the sheet plane, which is difficult to detect in the plane-view observation. Dislocation cores may be available at least near the boundaries of antiphase domains. However, dislocations with Burger's vectors other than those parallel to the layer plane could be less stable in such ultrathin nanosheets and have been annihilated at surfaces.

In the present perovskite-type niobate nanosheets, an interesting loop structure is discovered, which may be generated during the exfoliation process. Figure 7 shows the dark-field images of loops with different operating reflections. By noting that the lines of no contrast in the loops are always perpendicular to the corresponding \mathbf{g} vector, we conclude that the Burger's vector is normal to the layer plane, i.e., along the c axis. Quantitative EDS analysis has not found a significant difference in composition at the region of loops, i.e., it is close to the average Ca/Nb ratio of 0.420. It should be noted that the present loops show a somewhat different contrast compared to the pure dislocation loops.²⁷ The shape and the contrast are more like those of secondary precipitates.²⁸ However, microdiffraction and HREM analysis did not reveal a different crystal structure from the layered perovskite. Thus, the loop contrast could have resulted from the local collapse of crystal structure. The collapsed region exhibits a disk shape with a uniform diameter of 50 nm. The strain field due to the local collapse gave rise to the contrast of loop shape, which is similar to the vacancy-type dislocation loops.

The collapsed region could be either agglomerates of vacancies or loss of portions of crystal due to the destructive effects of preparation processes. By noting the fact that these loops do not show significant difference in composition and they are stable under electron irradiation, the loops are rather a destructive portion of crystal than agglomerates of vacancies. Though the precise structural model of the loops cannot be established based on the available information, it may be reasonable to consider that intercalation and exfoliation process may have washed away portions of the "soft" perovskite layers, leading to the collapse of local structure. This has been confirmed by the cross-section images in Figure 2. Thereafter, for example, two-layered perovskite slabs other than the original three-layered configuration may appear in some regions. Diffusion and agglomeration of cavities on the surface give rise to an energetically favored disc shape. Although the local collapse of the perovskite is similar to the structure of vacancy loops, the formation vector of the loop is not a rigid lattice vector in this layered structure although it has the magnitude of $[001]_c$.

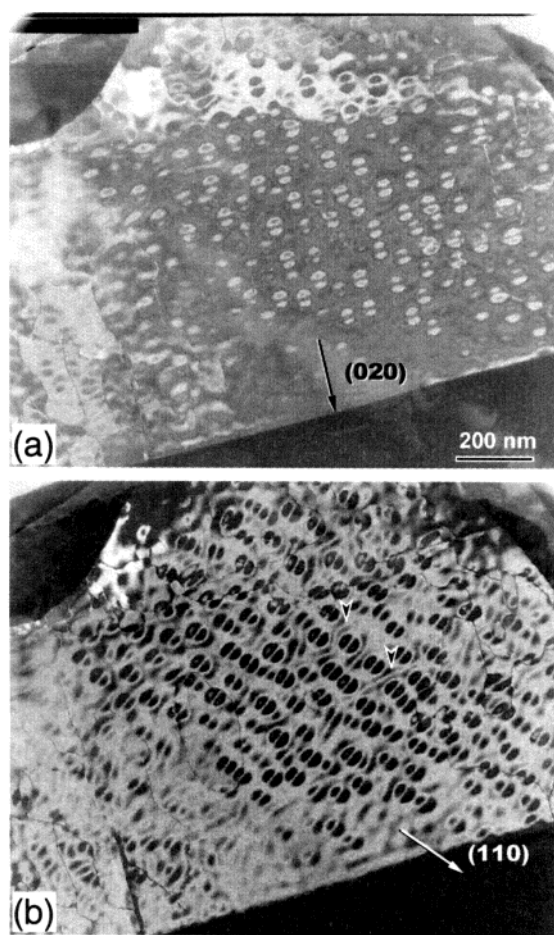


Figure 7. Dark-field images showing high density of loop contrast. Images were obtained by (a) the (020) and (b) the (110) operating reflections.

in the cubic perovskite. This has led to the appearance of a precipitate-like contrast rather than the pure dislocation loops. However, such a severe structural collapse, i.e., high density of loops, could not often be observed in the present TEM examination. The majority of layered perovskite crystallites have been exfoliated before catastrophic damage.

Restacking of Nanosheets. Restacking of nanosheet aggregates has been observed presently probably due to the drying process when the TEM specimen was prepared. Investigation of interfacial structures after restacking of nanosheets is very important since this is a common problem encountered in the practical application of this kind of material, e.g., chemical self-assembly into nanosized composites. Restacking was believed to occur by accommodating water and TBA molecules between the perovskite slabs. TEM always observed moiré fringes, which apparently carry information on the restacked structures.

Figure 8 shows different moiré patterns appearing within an individual fragment. The small restacked nanosheets are clearly outlined by the fringe contrast. All these moiré patterns are rotation type but with different rotation angles around the *c* axis. The rotation angle (α) can be determined according to the equation²⁹

$$\alpha = d/D \quad (2)$$

where *d* is the interplanar distance of a certain plane contributing to the imaging of moiré patterns and *D* is the span of the bright or dark fringes in the moiré pattern. A large *D* value corresponds

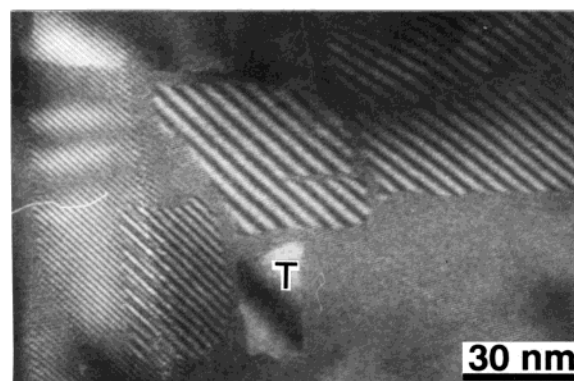


Figure 8. Moiré patterns due to restacking of nanosheets.

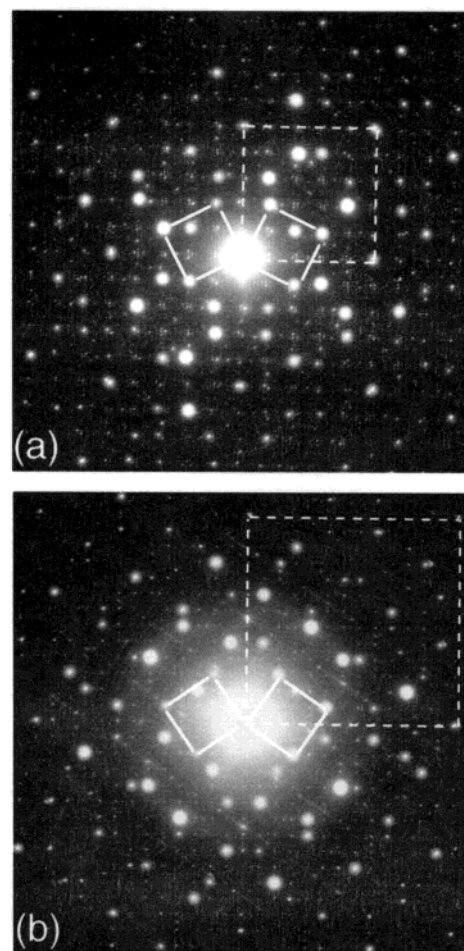


Figure 9. Diffraction patterns of (a) $\Sigma 5$ and (b) $\Sigma 13$ interfaces of restacked nanosheets.

to a small α . It is found that most nanosheets rotate by an angle of no more than 0.3 rad around the sheet normal when restacking onto one another. The tiny restacked nanosheet indicated by “T” in Figure 8 shows different contrast from the matrix fragment under the DF image condition, but no moiré fringes appear. This small nanosheet was attached with a critically identical orientation, but a lattice displacement was involved in a certain direction parallel to the nanosheet surface.

Restacking via large-angle rotation is also discovered, as indicated by diffraction patterns shown in Figure 9. The rotation angles are 36.9° and 22.6° for parts a and b of Figure 9, respectively. These two angles are special ones that correspond to $\Sigma 5$ and $\Sigma 13$ coincidence site lattice (CSL), respectively. The CSL for each specific interfacial structure is outlined by dashed

lines in Figure 9. Whether these special CSL categories were related to low-energy interfacial configurations is still unknown. At any rate, restacking of the present niobate perovskite-type nanosheets was found to employ regular configurations: small-angle rotation interface, CSL interface, or parallel interface with a lattice displacement. Restacking by random configuration was only observed in the case that two large and thick nanosheet aggregates restacked.

Acknowledgment. The authors wish to thank Dr. L. Bourgeois in Monash University (Australia) for reading the manuscript and providing useful suggestions and Dr. Y. Gao in NIMS for helpful discussion. We acknowledge Dr. M. Mitome and Mr. K. Kurashima in NIMS for technical assistance in TEM work.

References and Notes

- (1) Jacobson, A. J.; Lewandowski, J. T.; Johnson, J. W. *J. Less-Common Met.* **1986**, *116*, 137.
- (2) (a) Sasaki, T.; Watanabe, M.; Michiue, Y.; Komatsu, Y.; Izumi, F.; Takenouchi, S. *Chem. Mater.* **1995**, *7*, 1001. (b) Sasaki, T.; Kooli, F.; Iida, M.; Michiue, Y.; Takenouchi, S.; Yajima, Y.; Izumi, F.; Chakoumakos, B. C.; Watanabe, M. *Chem. Mater.* **1998**, *10*, 4123.
- (3) (a) Brock, S. L.; Sanabria, M.; Nair, J.; Suib, S. L.; Ressler, T. J. *Phys. Chem. B* **2001**, *105*, 5404. (b) Crosnier-Lopez, M. P.; Le Berre, F.; Fourquet, J. L. *J. Mater. Chem.* **2001**, *11*, 1146.
- (4) Treacy, M. M. J.; Rice, S. B.; Jacobson, A. J.; Lewandowski, J. T. *Chem. Mater.* **1990**, *2*, 279.
- (5) Jacobson, A. J. *Mater. Sci. Forum* **1994**, *152–153*, 1.
- (6) (a) Sasaki, T.; Watanabe, M.; Hashizume, H.; Yamada, H.; Nakazawa, H. *J. Am. Chem. Soc.* **1996**, *118*, 8329. (b) Sasaki, T.; Watanabe, M. *J. Am. Chem. Soc.* **1998**, *120*, 4682.
- (7) (a) Schaak, R. E.; Mallouk, T. E. *Chem. Mater.* **2000**, *12*, 2513. (b) Schaak, R. E.; Mallouk, T. E. *Chem. Mater.* **2000**, *12*, 3434.
- (8) (a) Han, Y. S.; Park, I.; Choy, J. H. *J. Mater. Chem.* **2001**, *11*, 1277. (b) Sukpirom, N.; Lerner, M. M. *Chem. Mater.* **2001**, *13*, 2179.
- (9) (a) Nakato, T.; Furumi, Y.; Okuhara, T. *Chem. Lett.* **1998**, 611. (b) Kaschak, D. M.; Johnson, S. A.; Hooks, D. E.; Kim, H. N.; Ward, M. D.; Mallouk, T. E. *J. Am. Chem. Soc.* **1998**, *120*, 10887.
- (10) Saupe, G. B.; Waraksa, C. C.; Kim, H. N.; Han, Y. J.; Kaschak, D. M.; Skinner, D. M.; Mallouk, T. E. *Chem. Mater.* **2000**, *12*, 1556.
- (11) Sasaki, T.; Ebina, Y.; Kitami, Y.; Watanabe, M. *J. Phys. Chem. B* **2001**, *105*, 6116.
- (12) (a) Sasaki, T.; Watanabe, M. *J. Phys. Chem. B* **1997**, *101*, 10159. (b) Sasaki, T.; Ebina, Y.; Watanabe, M.; Decher, G. *Chem. Commun.* **2000**, 2163.
- (13) (a) Ottschi, K. D.; Poeppelmeier, K. R.; Salvador, P. A.; Mason, T. O.; Zhang, H.; Marks, L. D. *J. Am. Chem. Soc.* **1996**, *118*, 8951. (b) Salvador, P. A.; Greenwood, K. B.; Mawdsley, J. R.; Poeppelmeier, K. R.; Mason, T. O. *Chem. Mater.* **1999**, *11*, 1760.
- (14) (a) Brahmrou, B.; Messing, G. L.; Troler-Mckinstry, S.; Selvaraj, U. In *Proceedings of the 10th IEEE International Symposium on Applications of Ferroelectrics*, Vol II; Kulwicki, B. M., Amin, A., Safari, A., Eds.; IEEE: Piscataway, NJ, 1996; pp 883–886. (b) Takeuchi, T.; Tani, T.; Satoh, T. *Solid State Ionics* **1998**, *108*, 67. (c) Horn, J.; Zhang, S. C.; Selvaraj, U.; Messing, G. L.; Troler-Mckinstry, S. *J. Am. Ceram. Soc.* **1999**, *82*, 921. (d) Rehrig, P. W.; Park, S.-E.; Troler-Mckinstry, S.; Messing, G. L.; Jones, B.; Shrout, T. R. *J. Appl. Phys.* **1999**, *86*, 1657.
- (15) (a) Takata, T.; Furumi, Y.; Shinohara, K.; Tanaka, A.; Hara, M.; Kondo, J. N.; Domen, K. *Chem. Mater.* **1997**, *9*, 1063. (b) Kim, H. G.; Hwang, D. W.; Kim, J.; Kim, Y. G.; Lee, J. S. *Chem. Commun.* **1999**, 1077.
- (16) Moritomo, Y.; Asamitsu, A.; Kuwahara, H.; Tokura, Y. *Nature* **1996**, *380*, 141.
- (17) Uma, S.; Gopalakrishnan, J. *Chem. Mater.* **1994**, *6*, 907.
- (18) Fang, M.; Kim, C. H.; Soupe, G. B.; Kim, H. N.; Waraksa, C. C.; Miwa, T.; Fujishima, A.; Mallouk, T. E. *Chem. Mater.* **1999**, *11*, 1526.
- (19) Xu, F. F.; Bando, Y.; Ebina, Y.; Sasaki, T. *Philos. Mag. A* **2002**, *82*, 2655.
- (20) Cliff, G.; Lorimer, G. W. *J. Microsc. (Oxford)* **1975**, *103*, 203.
- (21) MacTempas software package. Total Resolution: Berkeley, CA. <http://www.totalresolution.com/MacTempas.html>.
- (22) DigitalMicrograph. Gatan, Inc.: Pleasanton, CA. http://www.gatan.com/imaging/dig_micrograph.html.
- (23) Xu, F. F.; Ebina, Y.; Bando, Y.; Sasaki, T. *J. Phys. Chem. B* **2003**, *107*, 6698.
- (24) Dion, M.; Ganne, M.; Tournoux, M. *Mater. Res. Bull.* **1981**, *16*, 1429.
- (25) (a) Ogawa, S.; Watanabe, D.; Watanabe, H.; Komoda, T. *Acta Crystallogr.* **1958**, *11*, 872. (b) Glossop, A. B.; Pashley, D. W. *Proc. R. Soc. London* **1959**, *A250*, 132.
- (26) (a) Holman, R. L.; Cressman, P. J.; Revelli, J. F. *Appl. Phys. Lett.* **1978**, *32*, 280. (b) Ritz, V. H.; Bermudez, V. M. *Phys. Rev. B: Condens. Matter* **1981**, *24*, 5559.
- (27) (a) Price, P. B. *Philos. Mag.* **1960**, *5*, 873. (b) Groves, G. W.; Kelly, A. *Philos. Mag.* **1961**, *6*, 1527. (c) Mazey, D. J.; Barnes, R. S. *Philos. Mag.* **1962**, *7*, 1861.
- (28) Ashby, M. F.; Brown, L. M. *Philos. Mag.* **1963**, *8*, 1649.
- (29) Hashimoto, H.; Mannami, M.; Naiki, T. *Philos. Trans. R. Soc. London* **1961**, *A253*, 459.